ACS NANO

www.acsnano.org

Super-Resolution Diamond Magnetic Microscopy of Superparamagnetic Nanoparticles

Nazanin Mosavian, Forrest Hubert, Janis Smits, Pauli Kehayias, Yaser Silani, Bryan A. Richards, and Victor M. Acosta*

Cite This: *ACS Nano* 2024, 18, 6523−6532

ABSTRACT: **Scanning-probe and wide-field magnetic microscopes based on nitrogen-vacancy (NV) centers in diamond have enabled advances in the study of biology and materials, but each method has drawbacks. Here, we implement an alternative method for nanoscale magnetic microscopy based on optical control of the charge state of NV centers in a dense layer near the diamond surface. By combining a donut-beam super-resolution technique with optically detected magnetic resonance spectroscopy, we imaged the magnetic fields produced by single 30 nm iron-oxide nanoparticles. The magnetic microscope has a lateral spatial resolution of ∼100 nm, and it resolves the individual magnetic dipole features from clusters of nanoparticles with interparticle spacings down to ∼190 nm. The magnetic feature amplitudes are more than an order of magnitude larger than those obtained by confocal magnetic microscopy due to the narrower optical point-spread function and the shallow depth of NV centers. We analyze the magnetic nanoparticle images and sensitivity as a function of the microscope's spatial resolution and show that the signal-to-noise ratio for nanoparticle detection does not degrade as the spatial resolution improves. We identify sources of background fluorescence that limit the present performance, including diamond second-order Raman emission and imperfect NV charge state control. Our method, which uses <10 mW laser power and can be parallelized by patterned illumination, introduces a promising format for nanoscale magnetic imaging.**

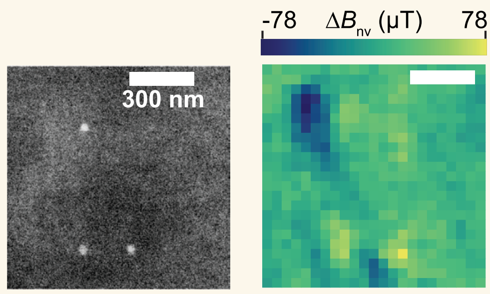

KEYWORDS: *quantum sensing, nitrogen vacancy centers, nanoscale magnetic imaging, super-resolution microscopy, superparamagnetic iron-oxide nanoparticles*

INTRODUCTION

Magnetic microscopes based on optically detected magnetic resonance (ODMR) spectroscopy of nitrogen-vacancy (NV) centers in diamond operate in a wide range of experimental conditions and offer a favorable combination of spatial resolution and sensitivity. One of the earliest demonstrations used a single NV center to image magnetic fields in a scanning-probe format.[1] The scanning-probe method has subsequently been applied to study numerous nanomagnetic samples,[2−8] with a spatial resolution down to ≲40 nm.[9] Wide-field magnetic microscopy using a dense, near-surface layer of NV centers has also emerged as a powerful tool, allowing for faster imaging and higher sensitivity.[10−15] Both methods have enabled notable advances in the study of biology[16,17] and materials,[9,18−21] but they have different drawbacks. The scanning-probe method requires a relatively complex apparatus and slow point-by-point scanning, while the widefield diamond magnetic microscope is limited by optical diffraction to a spatial resolution of ∼300 nm.[7,22]

An intriguing alternative NV magnetic-imaging technique involves the use of far-field super-resolution microscopy methods to achieve subdiffraction resolution.[23−39] However, to date, most demonstrations have required either high laser power or low NV density and were limited to the study of a small number of NV centers. Several works,[27,28,30,34,39] including those based on single-NV localization methods,[31,36] were able to resolve a few NV centers separated by a subdiffraction distance and measured their local magnetic fields. However, this type of sparse sampling does not provide a clear path toward super-resolution magnetic imaging with an array of many pixels. In order to generate a large nanoscale

Received: December 6, 2023
Revised: February 8, 2024
Accepted: February 12, 2024
Published: February 19, 2024

https://doi.org/10.1021/acsnano.3c12283
ACS Nano 2024, 18, 6523−6532

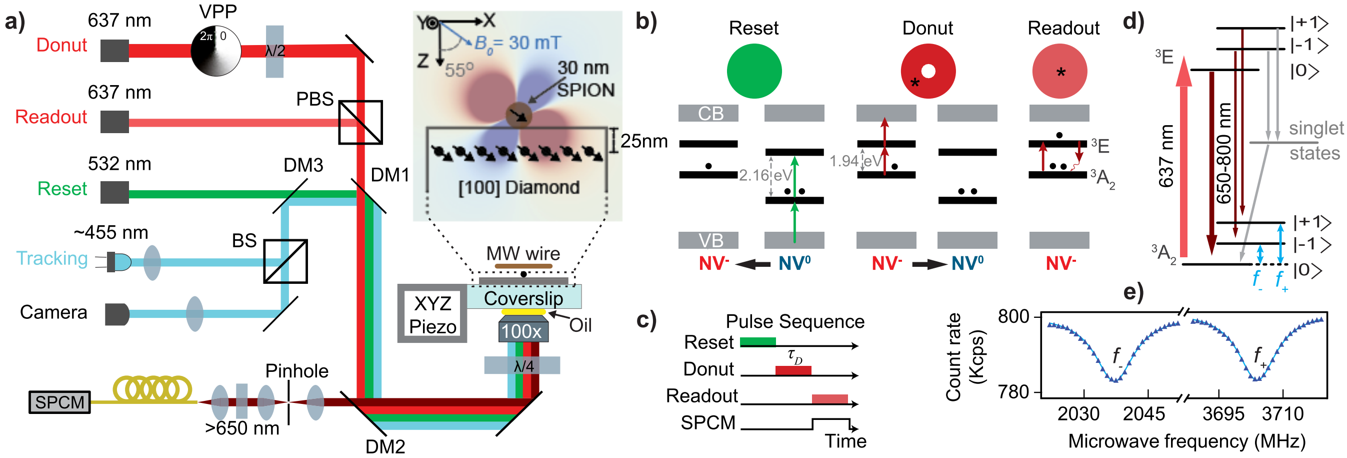

Figure 1. Super-resolution magnetic microscopy with NV centers. (a) Three collimated laser beams are combined using polarizing beam splitters (PBS) and dichroic mirrors (DM). Telescopes are used to expand each beam's diameter to ≳0.5 cm to match the back aperture of the objective. A vortex phase plate (VPP) is used to create the donut-shaped mode of the Donut beam. A $\lambda/4$ waveplate is used to generate the circular polarization needed to preserve the Donut beam's profile under tight focusing.[40] Emission is spatially filtered with a pinhole, spectrally filtered, and detected with an avalanche-photodiode single-photon counting module (SPCM). The diamond membrane is glued to a glass coverslip, and SPION samples are dispersed on the opposite side of the diamond that hosts a dense ~25 nm deep layer of NV centers. The assembly is scanned using a closed-loop piezoelectric nanopositioning stage, and a blue LED reflectance imaging system is used to minimize sample drift. Inset: depiction of the *xz*-plane magnetic field profile of a single SPION. (b) Allowed NV^0 and NV^- optical transitions for each step of the CSD microscopy sequence. (c) Pulse sequence used for CSD microscopy. (d) Energy levels and optical and spin transitions of the NV^- center. (e) Experimental confocal ODMR spectrum ($\tau_D = 0$) at $B_0 = 30$ mT. Lorentzian fits (blue) of the $f_\pm$ center frequencies are used to determine B_{nv}.

array, a method that works with a high density of NV centers is required. A super-resolution method based on shelving in the NV metastable singlet state[27,39] has been used to resolve two NV centers separated by ~100 nm and perform magnetometry on each.[39] However, this method is not compatible with high NV density because unavoidable background fluorescence causes the ODMR contrast to shrink as $1/N$, where N is the number of NV centers within a diffraction-limited laser spot.[28] Stimulated-emission depletion (STED) microscopy can in principle work at high NV density[28,30] and has been used to acquire ODMR spectra of five NV centers separated by 150−300 nm.[28] However, this required a very high depletion laser power (≳1 W for ~50 nm resolution[28]), due in part to the small NV stimulated-emission cross section,[23] restricting the samples that can be studied.

One method, called charge-state depletion (CSD) microscopy,[25,34,35,37,38] involves the use of a donut beam to drive most NV centers into their neutrally charged NV^0 "dark state" while leaving a subwavelength-sized core at the center in the negatively charged NV^- sensing state. This method has the benefit of using relatively low laser power (at least 2 orders of magnitude lower than STED[25]) and retaining high ODMR contrast for the NV^- centers in the core, even when using dense near-surface layers of NV centers.[35] CSD microscopy was previously used to map changes in ODMR contrast due to the microwave field produced by proximal silver nanowires, with a feature width, ~290 nm full-width-at-half-maximum (fwhm), narrower than that observed by confocal microscopy.[35]

In this paper, we demonstrate application of the CSD technique to perform super-resolution magnetic microscopy. We imaged the magnetic field produced by 30 nm superparamagnetic iron-oxide nanoparticles (SPIONs) with a lateral resolution of ~100 nm. The improved resolution is also accompanied by a more than 10-fold increase in the magnetic feature amplitude. We identify sources of background light that limit the present performance due to diamond Raman emission and imperfect charge-state control. Our microscope uses <10 mW of laser power and can be parallelized with a multidonut illumination scheme,[41,42] offering a path toward high-speed nanoscale magnetic microscopy.

RESULTS AND DISCUSSION

Experimental Setup. The experimental apparatus is depicted in Figure 1a (see also Methods section). Three laser beams are combined for interrogating NV centers: two at 637 nm ("Donut" and "Readout") and one at 532 nm ("Reset"). The laser beams are overlapped and directed to a confocal microscope with a 1.3 nm numerical aperture oil-immersion objective. In the focal plane of the microscope is a dense layer of NV centers, ~25 nm from the surface of a ~80 μm thick electronic-grade diamond membrane (section SI). A microwave wire is positioned on top of the diamond for driving the spin transitions of NV^- centers. NV^- emission is spectrally filtered (passing >650 nm) and detected with a single-photon-counting avalanche photodiode. Samples are scanned using a closed-loop *XYZ* piezoelectric nanopositioner, and a blue LED imaging system is used to track fiducial markers milled into the diamond substrate, limiting drift to ≲30 nm/day (section SII).

Figure 1b depicts the working principle of CSD microscopy.[25,34,35,37,38] The 637 nm Donut beam photoionizes NV centers in the high-intensity region of the beam into the NV^0 charge state, leaving a small subwavelength core at the beam's center where NV centers remain in the NV^- state. The low-power Gaussian-shaped Readout beam selectively excites NV^- centers in the core, but its 637 nm wavelength is too long to excite NV^0 centers in the periphery. The 532 nm Gaussian-shaped Reset beam initializes all NV centers to an equilibrium charge-state distribution, where typically most NV centers are in the NV^- state.[43−45] The three beams are applied in sequential μs-scale pulses, Figure 1c, and the single-photon

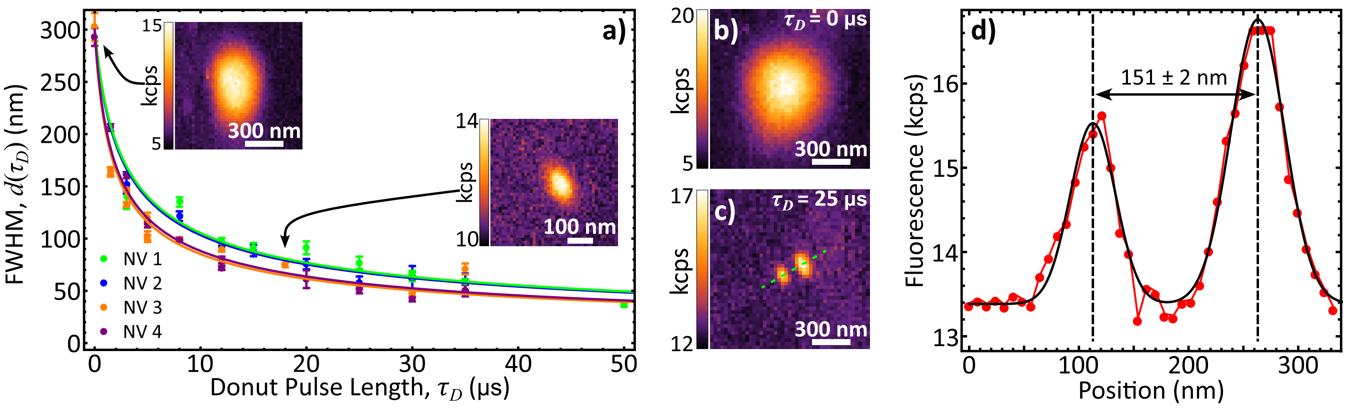

Figure 2. CSD resolution enhancement. (a) Lateral fwhm of CSD profiles of four individual NV centers as a function of the Donut beam pulse length. The solid colored lines are fits to eq 1. The fitted values of τ_{sat} for each NV center {NV1, NV2, NV3, NV4} are τ_{sat} = {1.35 ± 0.07 μs, 1.40 ± 0.14 μs, 0.87 ± 0.05 μs, 0.94 ± 0.07 μs}, respectively. Insets are two example images used in the data set. (b, c) Images of an NV cluster taken by (b) confocal microscopy (τ_D = 0 μs) and (c) CSD microscopy (τ_D = 25 μs). (d) CSD fluorescence rate along the dashed line annotated in (c). These linecut data were taken from a finer-sampled (300 nm × 300 nm) image of the same region using a 30 μs donut pulse length. The black solid line is a fit to two Gaussian functions, revealing an NV center separation of 151 ± 2 nm.

counting electronics count only photons during the Readout pulse (see the Methods section).

Figure 1d depicts the energy levels and transitions of the NV^- center that allow for magnetic field detection. A combination of optical polarization, spin-dependent fluorescence, and resonant microwave driving of the NV^- spin transitions enables ODMR spectroscopy.[46] An example ODMR spectrum is shown in Figure 1e, revealing two peaks that are fit to Lorentzian functions. The fitted central frequencies, $f_\pm$, are related to the magnetic field component along the NV axis by $B_{nv} \approx (f_+ - f_-)/(2\gamma_{nv})$, where γ_{nv} = 28.03 GHz/T is the NV electron-spin gyromagnetic ratio. The magnetic field produced by the sample is then $\Delta B_{nv} = B_{nv} - B_0$, where B_0 = 30 mT is the applied bias field along the NV axis.

CSD Optical Point Spread Function. We first characterized the optical point-spread function of our CSD microscope using a diamond with a low density of NV centers located within ∼1 μm of the surface.[47,69] For these experiments, a 0.36 mW Reset beam was applied for 5 μs, a 9.8 mW Donut beam was applied for a variable time τ_D, and a 0.12 mW Readout beam was applied for 40 μs (section SIII). We recorded CSD images of four isolated NV centers for different values of the donut pulse length, τ_D. For each fluorescence image, we take a horizontal linecut and fit the intensity profile to a Gaussian function to extract the lateral fwhm, $d(\tau_D)$. Figure 2a shows the fitted $d(\tau_D)$ for each of the four NV centers. In the absence of a Donut beam, the lateral fwhm is d = 296 ± 7 nm. For a donut pulse of length τ_D = 50 μs, the lateral fwhm is d = 37 ± 2 nm (section SIV), which represents an 8-fold resolution narrowing. At this pulse length, we also observe a ∼4-fold reduction in peak fluorescence amplitude, likely due to imperfect donut intensity contrast,[48] and a ∼3-fold increase in background fluorescence (section SV).

The data in Figure 2a are well described by the function:[25,37]

$$d(\tau_D) = \frac{d_0}{\sqrt{1 + \frac{\tau_D}{\tau_{sat}}}} \tag{1}$$

where d_0 = 300 nm is a fixed parameter representing the diffraction-limited confocal resolution and τ_{sat} is a fit parameter. From the fits, we extract an ensemble-averaged value τ_{sat} = 1.04 ± 0.27 μs for the 4 NV centers (section SV).

We also used our CSD microscope to resolve a pair of NV centers spaced closer than the optical diffraction limit. Figure 2b,c shows images of an NV cluster taken by confocal microscopy (τ_D = 0 μs) and CSD microscopy (τ_D = 25 μs), respectively. Only the CSD image is able to resolve the two NV centers. Figure 2d shows a linecut from a zoomed-in CSD image. Gaussian fits reveal that the NV centers are separated by 151 ± 2 nm.

Super-Resolution Magnetic Microscopy. We performed super-resolution magnetic microscopy of SPIONs by combining ODMR spectroscopy and CSD microscopy on a diamond with a high planar density of NV centers ($\gtrsim 10^3$ μm^{-2}) located ∼25 nm from the surface (section SI). SPIONs form convenient test samples[14] because they effectively behave as point-like dipoles with a magnetic moment that can be controlled by moderate magnetic fields. This is due to their small size (∼30 nm diameter, section SVI) and superparamagnetic behavior. At B_0 = 30 mT, the SPION magnetization is small enough that magnetic-field gradients do not meaningfully broaden the NV ODMR lines under confocal magnetic microscopy. However, with super-resolution magnetic microscopy, SPION gradients do have an effect on the ODMR lineshapes, adding additional information;[49] see section SIX.

A SPION suspension is drop-cast on the diamond surface at a suitable concentration such that both isolated SPIONs ($\gtrsim$1 μm between nearest neighbors) and clusters of SPIONs ($\lesssim$300 nm between nearest neighbors) are present in different regions (section SVI). To correlate scanning electron microscopy (SEM) with super-resolution magnetic microscopy images, we etched fiducial markers into the diamond using focused ion beam milling (section SI). The fiducial markers are resolved by SEM, fluorescence, and blue reflectance imaging.

Figure 3a shows an SEM image of a single isolated SPION on the diamond surface. Figure 3b shows magnetic images of the same SPION with and without the Donut beam applied. Linecuts through the images are shown in Figure 3c. To form a magnetic image, the sample is moved to a desired position, and the CSD pulse sequence in Figure 1c is continuously repeated. For all magnetic imaging experiments, a 0.4 mW Reset is

https://doi.org/10.1021/acsnano.3c12283
ACS Nano 2024, 18, 6523−6532

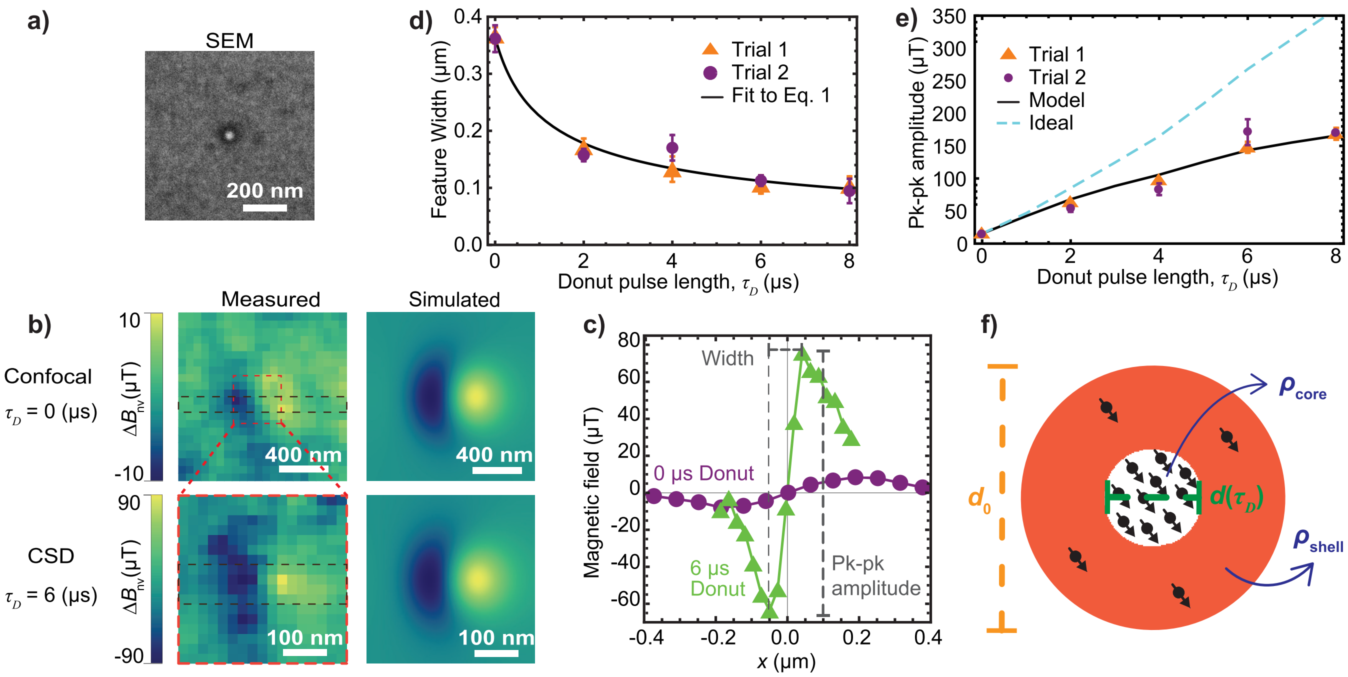

Figure 3. Super-resolution magnetic microscopy of single SPIONs. (a) SEM image of a single SPION on top of the diamond. (b) Top: confocal magnetic image ($\tau_D = 0$) of the SPION in (a) along with a simulated profile (section SVII). Bottom: CSD super-resolution magnetic image ($\tau_D = 6$ μs) of the same SPION and simulated profile. (c) Horizontal linecuts through the magnetic images, as indicated in (b). The definitions of the magnetic feature width and peak-to-peak (pk-pk) amplitude are annotated with dashed lines. (d) Feature width of SPION magnetic images acquired at several values of τ_D (labeled Trials 1 and 2). For redundancy, two images were acquired for each value of τ_D. The black curve is a fit to eq 1 (see section SVIII), with $\tau_{sat} = 0.63 \pm 0.08$ μs and $d_0 = 0.36 \pm 0.01$ μm. (e) Magnetic pk-pk feature amplitude as a function of τ_D for the same SPION magnetic images as in (d). The dashed cyan curve is the result of simulations where the SPION magnetization is constant and the NV$^-$ distribution follows the ideal behavior of eq 1 with $\tau_{sat} = 0.63$ μs (section SVIII). The solid black curve is a model that incorporates a nonzero density of NV$^-$ centers in the high-intensity region of the Donut beam, with a shell/core density ratio $\rho_{shell}/\rho_{core} = 0.15$. (f) Schematic of the model used for the black curve in (e). We also obtained CSD magnetic images of ferromagnetic nanoparticles, with qualitatively similar results (section SX).

applied for 5 μs, a 9.8 mW Donut is applied for a variable time τ_D, and a 0.2 mW Readout is applied for 20 μs. Meanwhile, the microwave frequency is slowly swept (sweep time, 20 ms; span, 30 MHz) (first about the f_- transition and then about the f_+ transition) to obtain ODMR spectra. The microwave sweeps are repeated, and ODMR spectra are averaged together for a total pixel dwell time (1−100 s) that is sufficient to determine $f_\pm$ and compute ΔB_{nv} for that location. The diamond-SPION sample is then moved to the next location, and the process is repeated pixel-by-pixel until an image is formed and processed (section SVII).

With the Donut beam off ($\tau_D = 0$), the SPION magnetic feature in Figure 3b,c has a peak-to-peak amplitude of 14.3 ± 0.8 μT and a width, 366 ± 12 nm, that is limited by optical diffraction of the confocal microscope. With the Donut beam on ($\tau_D = 6$ μs), the feature amplitude grows to 131 ± 8 μT and the width narrows to 111 ± 8 nm.

The dramatic increase in magnetic feature amplitude observed with super-resolution magnetic microscopy is a result of the rapid decay of the SPION magnetic field with distance. We model the SPION as a point dipole, with a magnetic moment $\vec{m}$ parallel to both $\vec{B}_0$ and the relevant NV symmetry axis of our [100]-cut diamond; see Figure 1a. The component of the SPION magnetic field that produces shifts in the NV $f_\pm$ resonances is thus

$$\Delta B_{nv} = \frac{\mu_0 |\vec{m}|}{4\pi |\vec{r}|^5}(x^2 - y^2 + 2^{3/2}xz) \tag{2}$$

where μ_0 is the vacuum permeability and $\vec{r} = \{x, y, z\}$ is the SPION-NV displacement vector in the lab coordinate system defined in Figure 1a. In simulations, we assume the NV layer is a sheet with a vertical displacement $z = 40$ nm from the center of the SPION. The magnetic images produced by our microscope are approximately the convolution of the CSD optical point-spread function and the magnetic field in the $z = 40$ nm plane. Thus, even a moderate improvement in lateral spatial resolution, corresponding to a moderate reduction in characteristic values of $|\vec{r}|$, results in a large increase in the feature amplitude, see eq 2.

The observed magnetic features are reproduced by convolving eq 2 with a Gaussian kernel of lateral fwhm given by eq 1 ($\tau_{sat} = 0.63$ μs, $d_0 = 0.36$ μm), with only $|\vec{m}|$ as a free parameter (section SVIII). The simulated magnetic profiles are shown to the right of the experimental data in Figure 3b.

We acquired CSD magnetic images of the same SPION for different values of τ_D. Each image was processed as indicated in Figure 3c to extract the feature width and amplitude. Figure 3d shows the fitted feature width as a function of τ_D. At $\tau_D = 8$ μs, the feature width is 101 ± 13 nm, a factor of 3.6 ± 0.5 narrower than the confocal ($\tau_D = 0$) image. The data are fit to eq 1, yielding $\tau_{sat} = 0.63 \pm 0.08$ μs and $d_0 = 0.36 \pm 0.01$ μm.

Figure 3e shows the feature amplitude as a function of τ_D. At $\tau_D = 8$ μs, the feature amplitude is 156 ± 17 μT, a factor of 11 ± 1 increase over the confocal ($\tau_D = 0$) image. The dashed cyan curve indicates the expected amplitude obtained when fixing $|\vec{m}| = 0.86$ A·nm^2 at the value obtained from simulating

https://doi.org/10.1021/acsnano.3c12283
ACS Nano 2024, 18, 6523−6532

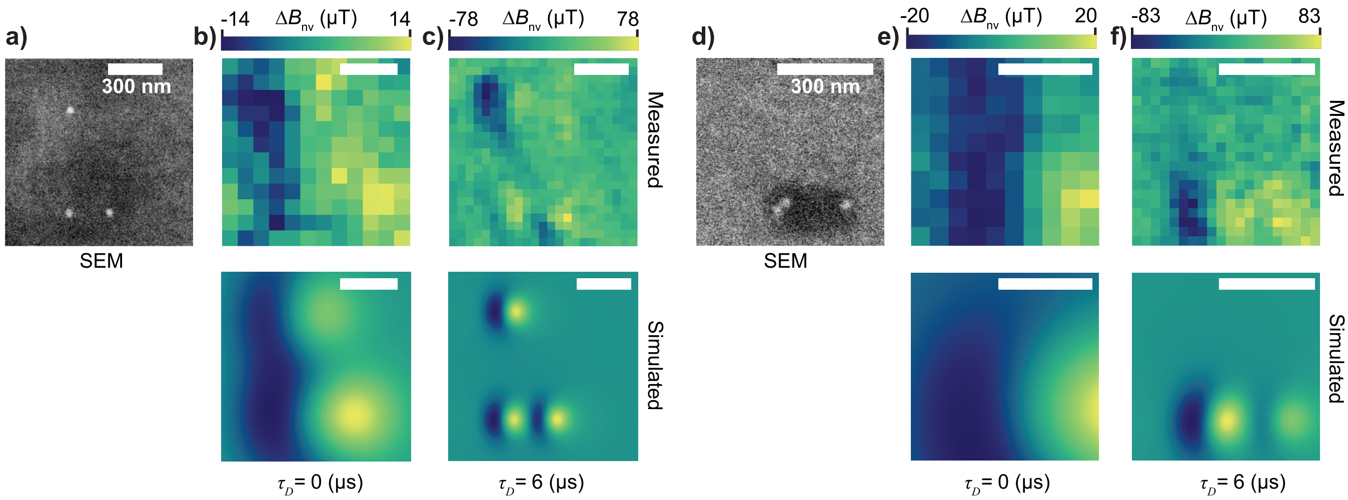

Figure 4. Super-resolution magnetic imaging of SPION clusters. (a) SEM image of a three-SPION cluster with the smallest interparticle spacing of 226 nm. (b) Experimental confocal magnetic image (top) along with simulation (bottom) of the cluster in (a). (c) CSD magnetic image (τ_D = 6 μs) and corresponding simulation. (d) SEM of another three-SPION cluster. The dark region is due to hexane residue. (e) Experimental confocal magnetic image and corresponding simulation of the region in (d). (f) CSD magnetic image (τ_D = 6 μs) and corresponding simulation. Additional information about this region of the sample is included in section SXI. All scale bars in (a)−(f) are 300 nm.

the confocal image and setting the Gaussian blur kernel's fwhm according to the $d(\tau_D)$ fit in Figure 3d.

While the amplitude observed in experiments, Figure 3e, increases by more than an order of magnitude from τ_D = 0 to τ_D = 8 μs, this is less than half of the expected increase. We attribute this discrepancy to imperfect control of the NV charge state.[45,50−53] As depicted in Figure 3f, in the high-intensity region of the donut, a small fraction of NV centers are not properly converted to NV^0 and exist as NV^- for at least a portion of the readout pulse. The resulting CSD magnetic images are then a weighted sum of the super-resolved magnetic image and a background confocal magnetic image (section SVIII):

$$\mathcal{I}_{tot} = (1 - \alpha)\mathcal{I}_{confocal} + \alpha\mathcal{I}_{superres} \quad (3a)$$

$$\alpha \approx \frac{1}{1 + \frac{\rho_{shell}}{\rho_{core}}\frac{\tau_D}{\tau_{sat}}} \quad (3b)$$

Here ρ_{shell} is the (undesired) NV^- density in the high-intensity donut "shell" and ρ_{core} is the (desired) NV^- density in the donut core. Expression 3 can be qualitatively understood as follows. As τ_D increases, the area of the donut core shrinks, and thus the number of NV^- centers in the core shrinks, while the number of undesired NV^- centers in the shell increases. The result is that the relative weight of the super-resolution image decreases with τ_D, reaching $\alpha \approx 0.4$ for τ_D = 8 μs. By comparing the experimentally observed amplitude with the expected values from the dashed cyan curve in Figure 3e, we infer a density ratio $\rho_{shell}/\rho_{core} \approx 0.15$; see section SVIII. The black curve in Figure 3e shows the simulated amplitude with $|\vec{m}|$ = 0.86 A·nm^2 fixed but allowing the relative weights of confocal and super-resolution images to vary according to expression 3.

We have found that imperfect charge-state control is a particularly acute problem when wavelengths shorter than 637 nm are used for the Readout beam. For example, with a 610 nm Readout (still longer than the ∼590 nm wavelength used in previous CSD microscopy studies[34,35,54−56]), at τ_D = 8 μs, we realize only a ∼2-fold narrowing in feature width and a ∼4-fold increase in amplitude compared to the confocal image. This effect may be attributed to the shorter Readout wavelengths converting NV^0 to NV^- through weak anti-Stokes excitation, leading to an increase in ρ_{shell}/ρ_{core}. CSD ODMR spectra obtained at different readout wavelengths further confirm this effect, see section SXIII. Our results indicate that a Readout wavelength below 637 nm may be suboptimal for CSD microscopy with a high density of NV centers. Further improvements in charge-state control will benefit from continued studies of the rich interplay of diamond sensor preparation and charge-state dynamics.[45,50−53] The background may be further suppressed by performing a weighted subtraction of the confocal magnetic image.[41]

Resolving SPION Clusters. Next, we performed super-resolution magnetic microscopy on clusters of SPIONs to demonstrate subdiffraction spatial resolution. Figure 4a,d shows SEM images of two different clusters, each containing three SPIONs. Confocal magnetic images of each region are shown in Figure 4b,e, along with their respective simulated profiles. CSD magnetic images (τ_D = 6 μs) of each region are shown in Figure 4c,f, along with their respective simulated profiles. The simulated magnetic profiles use the same parameters as in Figure 3b, with the relative dipole locations determined from the SEM images, and $|\vec{m}|$ is assumed to be the same for each SPION. For both regions, the confocal magnetic images contain a single broad magnetic feature and individual SPION features are not resolved. In the first region, Figure 4a−c, the CSD magnetic image contains three separate SPION features that are colocalized with the SEM image, with interparticle spacing down to 226 nm. In the second region, Figure 4d−f, the CSD magnetic image contains two colocalized SPION features spaced ∼190 nm apart. A very close pair of SPIONs spaced 37 nm apart is still not resolved. In both regions, the CSD magnetic image feature locations are in good agreement with the SEM image, as seen in the simulations.

Magnetic Sensitivity. The CSD magnetic images of SPION clusters in Figure 4c,f took approximately 1 day each to

https://doi.org/10.1021/acsnano.3c12283
ACS Nano 2024, 18, 6523−6532

acquire. Such long averaging times were required due to a relatively poor signal-to-noise ratio that degraded unexpectedly quickly with increasing τ_D. To investigate further, we studied the ODMR parameters relating to the magnetic sensitivity as a function of τ_D. The sensitivity is fundamentally limited by photon shot noise, with a minimum detectable magnetic field given by

$$B_{PSN} = \frac{4}{3\sqrt{3}} \frac{\Gamma}{\gamma_{NV} C \sqrt{I_0 \tau_{avg}}} \tag{4}$$

Here Γ is the ODMR fwhm, C is the contrast, I_0 is the fluorescence count rate, and τ_{avg} is the total acquisition time. Equation 4 is derived assuming the microwave frequency is tuned to the steepest slope of a Lorentzian ODMR peak. In our experiments, the microwave frequency is less-efficiently swept across the ODMR peaks, but the same scaling with Γ, C, and I_0 still applies.[11]

The sample was positioned in a SPION-free region, and ODMR spectra were acquired about each $f_\pm$ transition for different values of τ_D. Each spectrum was fit to a Lorentzian function to extract Γ, C, and I_0. Figure 5a shows the peak fluorescence rate, I_0, as a function of τ_D. A monotonic decrease in the fluorescence rate is observed. This qualitative behavior is expected because as τ_D increases, the number of NV^- in the donut core decreases. The observed behavior of $I_0(\tau_D)$ can be approximately described by the function

$$I_0(\tau_D) = I_0(0)\frac{d(\tau_D)^2}{{d_0}^2} + \text{bg} = \frac{I_0(0)}{1 + \frac{\tau_D}{\tau_{sat}}} + \text{bg} \tag{5}$$

where bg is a constant non-NV^- background, and in the last step we used eq 1. Fitting to the experimental data in Figure 5a, and applying $\tau_{sat} = 0.63$ μs from Figure 3d, we find $I_0(0) = 642 \pm 19$ kilocounts per second(kcps) and bg = 162 ± 9 kcps.

While the background fluorescence rate is relatively small compared to the NV^- fluorescence rate at $\tau_D = 0$, it nevertheless has a dramatic impact on the ODMR contrast for larger values of τ_D. Figure 5b shows the ODMR contrast, C, as a function of τ_D. At $\tau_D = 0$, the ODMR contrast is $C(0) = 2.2 \pm 0.1\%$, a fairly typical value for our high-NV-density, ion-implanted diamonds.[11,57] However, the ODMR contrast falls sharply with an increase in τ_D, eventually reaching $C(8\ \mu s) = 0.36 \pm 0.06\%$. This drop in contrast is largely due to the non-NV^- background, which becomes the dominant contribution to the fluorescence rate for $\tau_D \gtrsim 2$ μs, see Figure 5a. In order to fully describe our data, we found we also needed to include a term due to the "light-narrowing" effect of optical pumping by the Donut beam;[58,59] see section SXII. This choice is further justified by the decrease in Γ as a function of τ_D, Figure 5c, which is well described by the light-narrowing model. Additional details of the non-NV^- background and ODMR parameter modeling are in section SXII.

Using eq 4 and the parameters from Figure 5a−c, we calculated the photon-shot-noise-limited sensitivity, $\eta_{PSN} = B_{PSN}\sqrt{\tau_{avg}}$. The results are plotted in Figure 5d. The sensitivity degrades with increasing τ_D due to a combination of the (expected) decrease in I_0 and the (relatively unexpected) decrease in C arising from the non-NV^- background. A figure of merit for the signal-to-noise ratio in nanoparticle detection is defined as FOM = A/η_{PSN}, where A is the magnetic feature amplitude from Figure 3e. Figure 5e shows FOM as a function of τ_D for the experimental data, along with the ideal case

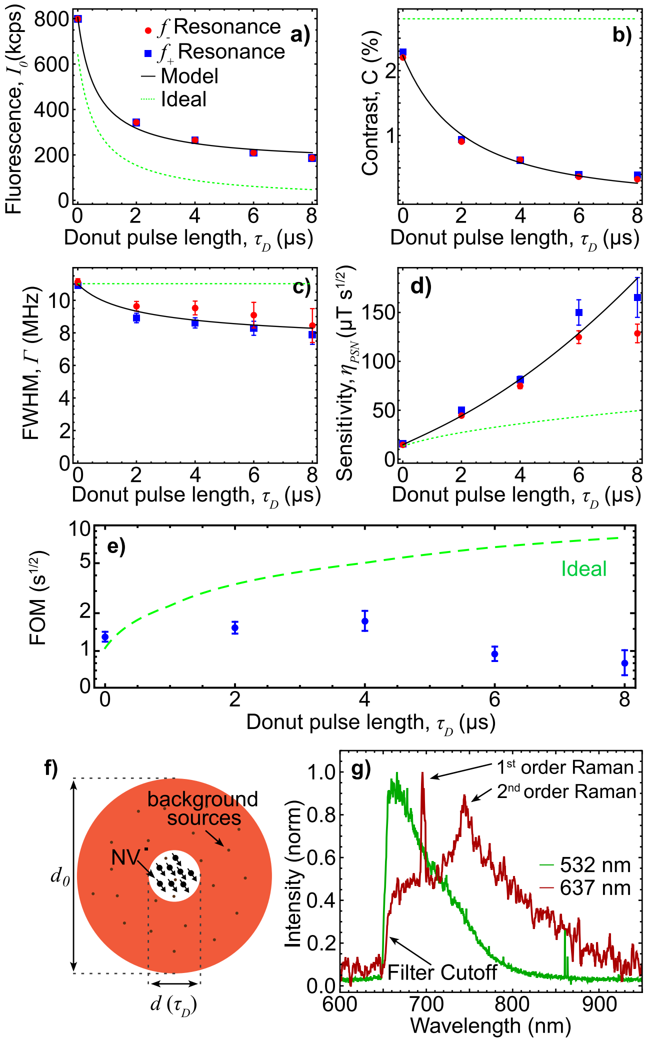

Figure 5. Magnetic sensitivity. **(a) Fluorescence rate, I_0, as a function of the donut pulse length, τ_D, for both $f_\pm$ ODMR resonances. (b) ODMR contrast, C, versus τ_D. (c) ODMR fwhm line width, Γ, versus τ_D. (d) Photon-shot-noise-limited sensitivity, calculated from eq 4, versus τ_D. (e) FOM versus τ_D. Blue points are calculated from experiments, and the dashed green curve is the simulated ideal case. In (a)−(d), solid black lines are a fit to a model that incorporates non-NV^- background, depicted in (f), as well as the light-narrowing effect (section SXII). In (a)−(e), the green dashed line is an extrapolation of the model fit assuming no background or light narrowing. (g) Fluorescence spectrum obtained with either 532 nm (green) or 637 nm (red) excitation. The annotated first and second order diamond Raman features appear only in the spectrum with 637 nm excitation.**

assuming no background fluorescence. In the present experiments, the FOM hardly changes, as the increase in feature amplitude with increasing τ_D is mostly offset by the degradation in sensitivity. However, the ideal case predicts that an ∼8-fold increase in FOM should be possible for $\tau_D = 8$ μs compared to the confocal case.

Our observations point to the need for minimizing sources of background fluorescence in future CSD experiments, as even a low background volume intensity can become substantial when the donut core is small, as depicted in Figure 5f. As a first step, we acquired fluorescence spectra under intense illumination to determine the nature of the background sources. Figure 5g shows spectra under 532 and 637 nm

https://doi.org/10.1021/acsnano.3c12283
ACS Nano 2024, 18, 6523−6532

illumination. For 532 nm illumination, the fluorescence spectrum appears as the typical broad phonon sideband of NV centers. However, under intense, continuous-wave 637 nm illumination, spectral features due to Raman emission of the diamond crystal[60] appear prominently. This suggests that diamond Raman emission contributes to the background observed in CSD ODMR spectra that limited our microscope's sensitivity (section SV). While the first-order Raman emission is sharp and could be spectrally filtered out, the second-order Raman emission is broad and covers much of the NV^- fluorescence collection band. Future experiments may benefit from time-gated fluorescence filtering,[61] exploiting the large difference between the diamond Raman emission lifetime ($\lesssim$10 ps[62]) and NV^- fluorescence lifetime (~10 ns[63]).

CONCLUSIONS

Our results represent an early step in the application of super-resolution microscopy methods to magnetic imaging and quantum sensing. Future improvements in spatial resolution and sensitivity can be realized by eliminating the non-NV^- background with time-gating[61] and reducing the undesired background NV^- fluorescence through improved diamond preparation and optical charge-state control.[45,50−53]

However, these improvements alone could only, at best, render the present technique on par with single-NV scanning probe methods. In order to realize comparable sensitivity to scanning probe methods over a continuously sampled image, $\gtrsim$10 NV centers per sensing voxel are required to maintain reasonable pixel-to-pixel uniformity and overcome the reductions in contrast and fluorescence collection efficiency typical of NV-ensemble measurements.[64] At an optimistic NV density of 10^{12} cm^{-2},[65] this implies a minimum pixel area of $\gtrsim(30\ nm)^2$, which is not a major improvement in spatial resolution over present scanning-probe methods.[9]

We expect the biggest improvements to come from parallelization of the image acquisition. As a relatively low-power, far-field super-resolution method, our technique is amenable to structured illumination methods that create arrays of thousands of donut-like modes over a wide field of view,[41,42] which could potentially provide a $\gtrsim$4 orders of magnitude speed-up in image acquisition.

With these improvements, high-speed nanoscale magnetic imaging over a wide field of view is within reach. Such a tool could enable a broad range of applications in materials science and biology. Examples of the latter include time-resolved studies of formation dynamics of malarial hemozoin in response to chemical environment,[11] mechanical deformations of DNA in magnetic tweezer arrays,[66] or *in vitro* magnetic screening of SPIONs and smaller magnetic nanoparticles,[67,68] just to name a few.

In summary, we demonstrated super-resolution magnetic microscopy based on the charge-state depletion of diamond NV centers. We imaged the magnetic fields produced by 30 nm diameter SPIONs with a lateral spatial resolution of ~100 nm and a ~10-fold increase in magnetic feature amplitude compared to confocal microscopy. With future improvements in Raman background suppression, NV charge-state control, and multidonut parallelization, our technique offers a path toward high-speed nanoscale magnetic microscopy.

METHODS

A detailed diagram of the CSD magnetic microscope is shown in Figure 1a. Here we provide additional details. The Donut laser source is a Toptica iBEAM-smart-640-s. In order to generate the donut shape, we pass a collimated Gaussian-shaped beam through a 629.2 nm vortex phase plate (VPP-1a, VIAVI Solutions, formerly RPC Photonics). The Readout laser source is an MRL-III-640 (CNI Laser) with a maximum power of 50 mW. A band-pass filter (FF01-637/7-25, Semrock) is used to remove any amplified spontaneous emission. Waveplates are used to ensure the Readout and Donut beams have orthogonal linear polarization. A polarizing beam splitter (PBS202, Thorlabs) is used to combine the Readout and Donut beams. The Reset laser source is a pigtail laser diode (LP520-SF15, Thorlabs). The Reset beam is combined with Donut and Readout beams by using a dichroic mirror (DMLP550R, Thorlabs). To generate μs-scale pulses, the Donut uses current modulation embedded in the source, and the Readout and Reset beams are controlled with Acousto-Optic Modulators (AOMs) (Brimrose TEM-85-10−-532 and Gooch & Housego 3110-120, respectively).

The Reset, Readout, and Donut beams each have their own telescopes used to generate collimated beams with a diameter comparable to the ~6 mm back aperture of the microscope objective. After combination, all beams pass through a quarter waveplate (WPQ10ME-633, Thorlabs) that generates circular polarization with the correct handedness needed to avoid wavefront distortions of the Donut beam from high-NA focusing.[40] The laser beams are then focused with a 100×, NA = 1.3, oil immersion objective lens (1-U2B53522, Olympus). The same objective collects fluorescence, which then passes through a dichroic mirror (ZT640rdc, Chroma) and is focused by a 200 mm focal-length tube lens (ITL200, Thorlabs) onto a pinhole. For experiments with single NV centers (Figure 2), we used a 75 μm diameter pinhole, and for all other experiments a 100 μm diameter pinhole (P100K, Thorlabs) was used. Light exiting the pinhole is recollimated with a lens and passed through a 650 nm long-pass filter (FELH0650, Thorlabs) to isolate NV^- phonon-sideband emission. A final lens focuses the light into a multimode fiber (M31L01, Thorlabs), which is connected to an avalanche photodiode (SPCM-AQRH-13-FC, Excelitas) used for photon counting.

The photodetector output is connected to the counter input of a data acquisition card (NI USB-6363, National Instruments). Three-dimensional scanning of the sample is achieved by a piezoelectric nanopositioning stage (MAX311D, Thorlabs). The sample scanning is synchronized with the photon counter via the same data acquisition card to form images. A home-built LabVIEW program controls the entire sequence.

For ODMR spectroscopy, the magnetic field is generated by a permanent magnet aligned with one of the NV orientations in the diamond sample. A copper wire placed above the diamond sensor is used to deliver microwaves. A microwave signal generator (Stanford Research Systems, SG384) is used to sweep microwaves about each ODMR transitions ($f_- \approx 2046$ MHz, $f_+ \approx 3699$ MHz). The microwaves are amplified (ZHL16W-43-S+, Mini-circuits) prior to connection with the copper loop used for delivery. The data acquisition card and LabVIEW program synchronized the timing of the microwave sweep with the optical pulses, photon counting, and nanopositioning stage.

ASSOCIATED CONTENT

Supporting Information

The Supporting Information is available free of charge at https://pubs.acs.org/doi/10.1021/acsnano.3c12283.

Diamond sensor preparation, image stabilization, laser pulse optimization, CSD amplitude and background, SPION sample preparation, magnetic profile simulations, SPION magnetic field gradients, sensitivity modeling, readout wavelength dependence, and other details (PDF)

AUTHOR INFORMATION

Corresponding Author

Victor M. Acosta − *Center for High Technology Materials and Department of Physics and Astronomy, University of New Mexico, Albuquerque, New Mexico 87106, United States;* orcid.org/0000-0003-0058-9954; Email: vmacosta@unm.edu

Authors

Nazanin Mosavian − *Center for High Technology Materials and Department of Physics and Astronomy, University of New Mexico, Albuquerque, New Mexico 87106, United States*

Forrest Hubert − *Center for High Technology Materials and Department of Physics and Astronomy, University of New Mexico, Albuquerque, New Mexico 87106, United States*

Janis Smits − *Center for High Technology Materials and Department of Physics and Astronomy, University of New Mexico, Albuquerque, New Mexico 87106, United States*

Pauli Kehayias − *Sandia National Laboratories, Albuquerque, New Mexico 87185, United States;* orcid.org/0000-0002-7597-4358

Yaser Silani − *Center for High Technology Materials and Department of Physics and Astronomy, University of New Mexico, Albuquerque, New Mexico 87106, United States*

Bryan A. Richards − *Center for High Technology Materials and Department of Physics and Astronomy, University of New Mexico, Albuquerque, New Mexico 87106, United States*

Complete contact information is available at: https://pubs.acs.org/10.1021/acsnano.3c12283

Author Contributions

N.M., P.K., and V.M.A. conceived the idea and designed the experiments. F.H. and N.M. built the apparatus, acquired and analyzed data, and wrote the initial manuscript draft. B.A.R., Y.S., P.K., and J.S. assisted in sample preparation, apparatus optimization, and data interpretation. J.S. wrote the control software. V.M.A. supervised the project. All authors helped edit the manuscript.

Funding

This work was supported by the National Science Foundation (Grants DMR-1809800, CHE-1945148, and OIA-1921199), National Institutes of Health (Grant DP2GM140921), and Department of Energy (LDRD University Grant 218242).

Notes

The authors declare no competing financial interest.

ACKNOWLEDGMENTS

We gratefully acknowledge advice and support from L. Goncalves-Webster, N. Ristoff, M. D. Aiello, A. Berzins, M. Saleh Ziabari, A. Laraoui, J. T. Damron, A. Jarmola, A. S. Backer, and K. A. Lidke.

REFERENCES

(1) Balasubramanian, G.; Chan, I. Y.; Kolesov, R.; Al-Hmoud, M.; Tisler, J.; Shin, C.; Kim, C.; Wojcik, A.; Hemmer, P. R.; Krueger, A.; Hanke, T.; Leitenstorfer, A.; Bratschitsch, R.; Jelezko, F.; Wrachtrup, J. Nanoscale imaging magnetometry with diamond spins under ambient conditions. *Nature* **2008**, *455*, 648.

(2) Maletinsky, P.; Hong, S.; Grinolds, M. S.; Hausmann, B.; Lukin, M. D.; Walsworth, R. L.; Loncar, M.; Yacoby, A. A robust scanning diamond sensor for nanoscale imaging with single nitrogen-vacancy centres. *Nat. Nanotechnol.* **2012**, *7*, 320.

(3) Rondin, L.; Tetienne, J.-P.; Spinicelli, P.; Dal Savio, C.; Karrai, K.; Dantelle, G.; Thiaville, A.; Rohart, S.; Roch, J.-F.; Jacques, V. Nanoscale magnetic field mapping with a single spin scanning probe magnetometer. *Appl. Phys. Lett.* **2012**, *100*, 153118.

(4) Tetienne, J.-P.; Hingant, T.; Kim, J.-V.; Diez, L. H.; Adam, J.-P.; Garcia, K.; Roch, J.-F.; Rohart, S.; Thiaville, A.; Ravelosona, D.; Jacques, V. Nanoscale imaging and control of domain-wall hopping with a nitrogen-vacancy center microscope. *Science* **2014**, *344*, 1366.

(5) Rugar, D.; Mamin, H. J.; Sherwood, M. H.; Kim, M.; Rettner, C. T.; Ohno, K.; Awschalom, D. D. Proton magnetic resonance imaging using a nitrogen-vacancy spin sensor. *Nat. Nanotechnol.* **2015**, *10*, 120.

(6) Chang, K.; Eichler, A.; Rhensius, J.; Lorenzelli, L.; Degen, C. L. Nanoscale Imaging of Current Density with a Single-Spin Magnetometer. *Nano Lett.* **2017**, *17*, 2367.

(7) Ariyaratne, A.; Bluvstein, D.; Myers, B. A.; Jayich, A. C. B. Nanoscale electrical conductivity imaging using a nitrogen-vacancy center in diamond. *Nat. Commun.* **2018**, *9*, 2406.

(8) Thiel, L.; Wang, Z.; Tschudin, M. A.; Rohner, D.; Gutiérrez-Lezama, I.; Ubrig, N.; Gibertini, M.; Giannini, E.; Morpurgo, A. F.; Maletinsky, P. Probing magnetism in 2D materials at the nanoscale with single-spin microscopy. *Science* **2019**, *364*, 973.

(9) Marchiori, E.; Ceccarelli, L.; Rossi, N.; Lorenzelli, L.; Degen, C. L.; Poggio, M. Nanoscale magnetic field imaging for 2D materials. *Nature Reviews Physics* **2022**, *4*, 49.

(10) Glenn, D. R.; Lee, K.; Park, H.; Weissleder, R.; Yacoby, A.; Lukin, M. D.; Lee, H.; Walsworth, R. L.; Connolly, C. B. Single-cell magnetic imaging using a quantum diamond microscope. *Nat. Methods* **2015**, *12*, 736.

(11) Fescenko, I.; Laraoui, A.; Smits, J.; Mosavian, N.; Kehayias, P.; Seto, J.; Bougas, L.; Jarmola, A.; Acosta, V. M. Diamond Magnetic Microscopy of Malarial Hemozoin Nanocrystals. *Phys. Rev. Appl.* **2019**, *11*, 034029.

(12) Steinert, S.; Dolde, F.; Neumann, P.; Aird, A.; Naydenov, B.; Balasubramanian, G.; Jelezko, F.; Wrachtrup, J. High sensitivity magnetic imaging using an array of spins in diamond. *Rev. Sci. Instrum.* **2010**, *81*, 043705.

(13) Pham, L. M.; Le Sage, D.; Stanwix, P. L.; Yeung, T. K.; Glenn, D.; Trifonov, A.; Cappellaro, P.; Hemmer, P. R.; Lukin, M. D.; Park, H.; Yacoby, A.; Walsworth, R. L. Magnetic field imaging with nitrogen-vacancy ensembles. *New J. Phys.* **2011**, *13*, 045021.

(14) Gould, M.; Barbour, R. J.; Thomas, N.; Arami, H.; Krishnan, K. M.; Fu, K. M. C. Room-temperature detection of a single 19 nm super-paramagnetic nanoparticle with an imaging magnetometer. *Appl. Phys. Lett.* **2014**, *105*, 072406.

(15) Simpson, D. A.; Tetienne, J.-P.; McCoey, J. M.; Ganesan, K.; Hall, L. T.; Petrou, S.; Scholten, R. E.; Hollenberg, L. C. L. Magneto-optical imaging of thin magnetic films using spins in diamond. *Sci. Rep.* **2016**, *6*, 22797.

(16) Aslam, N.; Zhou, H.; Urbach, E. K.; Turner, M. J.; Walsworth, R. L.; Lukin, M. D.; Park, H. Quantum sensors for biomedical applications. *Nature Reviews Physics* **2023**, *5*, 157.

(17) Zhang, T.; Pramanik, G.; Zhang, K.; Gulka, M.; Wang, L.; Jing, J.; Xu, F.; Li, Z.; Wei, Q.; Cigler, P.; Chu, Z. Toward Quantitative Bio-sensing with Nitrogen-Vacancy Center in Diamond. *ACS Sensors* **2021**, *6*, 2077.

(18) Casola, F.; van der Sar, T.; Yacoby, A. Probing condensed matter physics with magnetometry based on nitrogen-vacancy centres in diamond. *Nat. Rev. Mater.* **2018**, *3*, 17088.

(19) Acosta, V. M.; Bouchard, L. S.; Budker, D.; Folman, R.; Lenz, T.; Maletinsky, P.; Rohner, D.; Schlussel, Y.; Thiel, L. Color Centers in Diamond as Novel Probes of Superconductivity. *Journal of Superconductivity and Novel Magnetism* **2019**, *32*, 85.

(20) Ho, K. O.; Shen, Y.; Pang, Y. Y.; Leung, W. K.; Zhao, N.; Yang, S. Diamond quantum sensors: from physics to applications on condensed matter research. *Functional Diamond* **2021**, *1*, 160.

(21) Xu, Y.; Zhang, W.; Tian, C. Recent advances on applications of NV^- magnetometry in condensed matter physics. *Photonics Research* **2023**, *11*, 393.
(22) Scholten, S. C.; Healey, A. J.; Robertson, I. O.; Abrahams, G. J.; Broadway, D. A.; Tetienne, J. P. Widefield quantum microscopy with nitrogen-vacancy centers in diamond: Strengths, limitations, and prospects. *J. Appl. Phys.* **2021**, *130*, 150902.
(23) Han, K. Y.; Willig, K. I.; Rittweger, E.; Jelezko, F.; Eggeling, C.; Hell, S. W. Three-dimensional stimulated emission depletion microscopy of nitrogen-vacancy centers in diamond using continuous-wave light. *Nano Lett.* **2009**, *9*, 3323.
(24) Rittweger, E.; Han, K. Y.; Irvine, S. E.; Eggeling, C.; Hell, S. W. STED microscopy reveals crystal colour centres with nanometric resolution. *Nat. Photonics* **2009**, *3*, 144.
(25) Han, K. Y.; Kim, S. K.; Eggeling, C.; Hell, S. W. Metastable dark states enable ground state depletion microscopy of nitrogen vacancy centers in diamond with diffraction-unlimited resolution. *Nano Lett.* **2010**, *10*, 3199.
(26) Pezzagna, S.; Wildanger, D.; Mazarov, P.; Wieck, A. D.; Sarov, Y.; Rangelow, I.; Naydenov, B.; Jelezko, F.; Hell, S. W.; Meijer, J. Nanoscale Engineering and Optical Addressing of Single Spins in Diamond. *Small* **2010**, *6*, 2117.
(27) Maurer, P. C.; Maze, J. R.; Stanwix, P. L.; Jiang, L.; Gorshkov, A. V.; Zibrov, A. A.; Harke, B.; Hodges, J. S.; Zibrov, A. S.; Yacoby, A.; Twitchen, D.; Hell, S. W.; Walsworth, R. L.; Lukin, M. D. Far-field optical imaging and manipulation of individual spins with nanoscale resolution. *Nat. Phys.* **2010**, *6*, 912.
(28) Wildanger, D.; Maze, J. R.; Hell, S. W. Diffraction Unlimited All-Optical Recording of Electron Spin Resonances. *Phys. Rev. Lett.* **2011**, *107*, 017601.
(29) Wildanger, D.; Patton, B. R.; Schill, H.; Marseglia, L.; Hadden, J. P.; Knauer, S.; Schönle, A.; Rarity, J. G.; O'Brien, J. L.; Hell, S. W.; Smith, J. M. Solid Immersion Facilitates Fluorescence Microscopy with Nanometer Resolution and Sub-Ångström Emitter Localization. *Adv. Mater.* **2012**, *24*, OP309.
(30) Arroyo-Camejo, S.; Adam, M. P.; Besbes, M.; Hugonin, J. P.; Jacques, V.; Greffet, J. J.; Roch, J. F.; Hell, S. W.; Treussart, F. Stimulated emission depletion microscopy resolves individual nitrogen vacancy centers in diamond nanocrystals. *ACS Nano* **2013**, *7*, 10912.
(31) Pfender, M.; Aslam, N.; Waldherr, G.; Neumann, P.; Wrachtrup, J. Single-spin stochastic optical reconstruction microscopy. *Proc. Natl. Acad. Sci. U. S. A.* **2014**, *111*, 14669.
(32) Yang, X.; Tzeng, Y.-K.; Zhu, Z.; Huang, Z.; Chen, X.; Liu, Y.; Chang, H.-C.; Huang, L.; Li, W.-D.; Xi, P. Sub-diffraction imaging of nitrogen-vacancy centers in diamond by stimulated emission depletion and structured illumination. *RSC Adv.* **2014**, *4*, 11305.
(33) Yang, B.; Fang, C.-Y.; Chang, H.-C.; Treussart, F.; Trebbia, J.-B.; Lounis, B. Polarization effects in lattice-STED microscopy. *Faraday Discuss.* **2015**, *184*, 37.
(34) Chen, X.; Zou, C.; Gong, Z.; Dong, C.; Guo, G.; Sun, F. Subdiffraction optical manipulation of the charge state of nitrogen vacancy center in diamond. *Light: Science & Applications* **2015**, *4*, e230.
(35) Chen, X.-D.; Li, D.-F.; Zheng, Y.; Li, S.; Du, B.; Dong, Y.; Dong, C.-H.; Guo, G.-C.; Sun, F.-W. Superresolution Multifunctional Sensing with the Nitrogen-Vacancy Center in Diamond. *Physical Review Applied* **2019**, *12*, 044039.
(36) Barbiero, M.; Castelletto, S.; Zhang, Q.; Chen, Y.; Charnley, M.; Russell, S.; Gu, M. Nanoscale magnetic imaging enabled by nitrogen vacancy centres in nanodiamonds labelled by iron-oxide nanoparticles. *Nanoscale* **2020**, *12*, 8847.
(37) Storterboom, J.; Barbiero, M.; Castelletto, S.; Gu, M. Ground-State Depletion Nanoscopy of Nitrogen-Vacancy Centres in Nanodiamonds. *Nanoscale Res. Lett.* **2021**, *16*, 44.
(38) Wang, Q.-Y.; Wang, Z.-H.; Du, B.; Chen, X.-D.; Guo, G.-C.; Sun, F.-W. Charge state depletion nanoscopy with a nitrogen-vacancy center in nanodiamonds. *Opt. Lett.* **2022**, *47*, 66.
(39) Jaskula, J.-C.; Bauch, E.; Arroyo-Camejo, S.; Lukin, M. D.; Hell, S. W.; Trifonov, A. S.; Walsworth, R. L. Superresolution optical magnetic imaging and spectroscopy using individual electronic spins in diamond. *Opt. Express* **2017**, *25*, 11048.
(40) Ganic, D.; Gan, X.; Gu, M. Focusing of doughnut laser beams by a high numerical-aperture objective in free space. *Opt. Express* **2003**, *11*, 2747.
(41) Chmyrov, A.; Keller, J.; Grotjohann, T.; Ratz, M.; d'Este, E.; Jakobs, S.; Eggeling, C.; Hell, S. W. Nanoscopy with more than 100,000 'doughnuts. *Nat. Methods* **2013**, *10*, 737.
(42) Yang, B.; Przybilla, F.; Mestre, M.; Trebbia, J.-B.; Lounis, B. Large parallelization of STED nanoscopy using optical lattices. *Opt. Express* **2014**, *22*, 5581.
(43) Aslam, N.; Waldherr, G.; Neumann, P.; Jelezko, F.; Wrachtrup, J. Photo-induced ionization dynamics of the nitrogen vacancy defect in diamond investigated by single-shot charge state detection. *New J. Phys.* **2013**, *15*, 013064.
(44) Chen, X.-D.; Li, S.; Shen, A.; Dong, Y.; Dong, C.-H.; Guo, G.-C.; Sun, F.-W. Near-Infrared-Enhanced Charge-State Conversion for Low-Power Optical Nanoscopy with Nitrogen-Vacancy Centers in Diamond. *Physical Review Applied* **2017**, *7*, 014008.
(45) Dhomkar, S.; Jayakumar, H.; Zangara, P. R.; Meriles, C. A. Charge Dynamics in near-Surface, Variable-Density Ensembles of Nitrogen-Vacancy Centers in Diamond. *Nano Lett.* **2018**, *18*, 4046.
(46) Acosta, V. M.; Budker, D.; Hemmer, P. R.; Maze, J. R.; Walsworth, R. L. Optical magnetometry with nitrogen-vacancy centers in diamond. In *Optical Magnetometry*; Budker, D., Jackson Kimball, D. F., Eds.; Cambridge University Press, 2013; pp 142−166.
(47) Santori, C.; Barclay, P. E.; Fu, K.-M. C.; Beausoleil, R. G. Vertical distribution of nitrogen-vacancy centers in diamond formed by ion implantation and annealing. *Phys. Rev. B* **2009**, *79*, 125313.
(48) Silani, Y.; Hubert, F.; Acosta, V. M. Stimulated Emission Depletion Microscopy with Diamond Silicon Vacancy Centers. *ACS Photonics* **2019**, *6*, 2577.
(49) Tetienne, J.-P.; Broadway, D. A.; Lillie, S. E.; Dontschuk, N.; Teraji, T.; Hall, L. T.; Stacey, A.; Simpson, D. A.; Hollenberg, L. C. L. Proximity-Induced Artefacts in Magnetic Imaging with Nitrogen-Vacancy Ensembles in Diamond. *Sensors* **2018**, *18*, 1290.
(50) Jayakumar, H.; Dhomkar, S.; Henshaw, J.; Meriles, C. A. Spin readout via spin-to-charge conversion in bulk diamond nitrogen-vacancy ensembles. *Appl. Phys. Lett.* **2018**, *113*, 122404.
(51) Yuan, Z.; Fitzpatrick, M.; Rodgers, L. V. H.; Sangtawesin, S.; Srinivasan, S.; de Leon, N. P. Charge state dynamics and optically detected electron spin resonance contrast of shallow nitrogen-vacancy centers in diamond. *Phys. Rev. Res.* **2020**, *2*, 033263.
(52) Olivares-Postigo, D.; Gorrini, F.; Bitonto, V.; Ackermann, J.; Giri, R.; Krueger, A.; Bifone, A. Divergent Effects of Laser Irradiation on Ensembles of Nitrogen-Vacancy Centers in Bulk and Nanodiamonds: Implications for Biosensing. *Nanoscale Res. Lett.* **2022**, *17*, 95.
(53) Giri, R.; Jensen, R. H.; Khurana, D.; Bocquel, J.; Radko, I. P.; Lang, J.; Osterkamp, C.; Jelezko, F.; Berg-Sorensen, K.; Andersen, U. L.; Huck, A. Charge Stability and Charge-State-Based Spin Readout of Shallow Nitrogen-Vacancy Centers in Diamond. *ACS Applied Electronic Materials* **2023**, *5*, 6603.
(54) Li, D.-F.; Du, B.; Chen, X.-D.; Guo, G.-C.; Sun, F.-W. Low power charge state depletion nanoscopy of the defect in diamonds with a pulsed laser excitation. *Opt. Lett.* **2020**, *45*, 730.
(55) Du, B.; Chen, X.-D.; Zhang, S.-C.; Dong, Y.; Li, C.-H.; Guo, G.-C.; Sun, F.-W. Fluorescence modulation of the nitrogen-vacancy center with competition between charge-state conversion and stimulated emission. *Journal of the Optical Society of America B* **2020**, *37*, 1468.
(56) Gardill, A.; Kemeny, I.; Li, Y.; Zahedian, M.; Cambria, M. C.; Xu, X.; Lordi, V.; Gali, A.; Maze, J. R.; Choy, J. T.; Kolkowitz, S. Super-Resolution Airy Disk Microscopy of Individual Color Centers in Diamond. *ACS Photonics* **2022**, *9*, 3848.
(57) Kehayias, P.; Jarmola, A.; Mosavian, N.; Fescenko, I.; Benito, F. M.; Laraoui, A.; Smits, J.; Bougas, L.; Budker, D.; Neumann, A.;

Brueck, S. R. J.; Acosta, V. M. Solution nuclear magnetic resonance spectroscopy on a nanostructured diamond chip. *Nat. Commun.* **2017**, *8*, 188.
(58) Dréau, A.; Lesik, M.; Rondin, L.; Spinicelli, P.; Arcizet, O.; Roch, J.-F.; Jacques, V. Avoiding power broadening in optically detected magnetic resonance of single NV defects for enhanced dc magnetic field sensitivity. *Phys. Rev. B* **2011**, *84*, 195204.
(59) Jensen, K.; Acosta, V. M.; Jarmola, A.; Budker, D. Light narrowing of magnetic resonances in ensembles of nitrogen-vacancy centers in diamond. *Phys. Rev. B* **2013**, *87*, 014115.
(60) Solin, S. A.; Ramdas, A. K. Raman Spectrum of Diamond. *Phys. Rev. B* **1970**, *1*, 1687.
(61) Faklaris, O.; Garrot, D.; Joshi, V.; Druon, F.; Boudou, J.-P.; Sauvage, T.; Georges, P.; Curmi, P. A.; Treussart, F. Detection of Single Photoluminescent Diamond Nanoparticles in Cells and Study of the Internalization Pathway. *Small* **2008**, *4*, 2236.
(62) Lee, K.; Sussman, B. J.; Nunn, J.; Lorenz, V.; Reim, K.; Jaksch, D.; Walmsley, I.; Spizzirri, P.; Prawer, S. Comparing phonon dephasing lifetimes in diamond using Transient Coherent Ultrafast Phonon Spectroscopy. *Diamond Relat. Mater.* **2010**, *19*, 1289.
(63) Collins, A. T.; Thomaz, M. F.; Jorge, M. I. B. Luminescence decay time of the 1.945 eV centre in type Ib diamond. *Journal of Physics C: Solid State Physics* **1983**, *16*, 2177.
(64) Tetienne, J.-P.; Lombard, A.; Simpson, D. A.; Ritchie, C.; Lu, J.; Mulvaney, P.; Hollenberg, L. C. L. Scanning Nanospin Ensemble Microscope for Nanoscale Magnetic and Thermal Imaging. *Nano Lett.* **2016**, *16*, 326.
(65) Kleinsasser, E. E.; Stanfield, M. M.; Banks, J. K. Q.; Zhu, Z.; Li, W.-D.; Acosta, V. M.; Watanabe, H.; Itoh, K. M.; Fu, K.-M. C. High density nitrogen-vacancy sensing surface created via He+ ion implantation of 12C diamond. *Appl. Phys. Lett.* **2016**, *108*, 202401.
(66) Kazi, Z.; Shelby, I. M.; Watanabe, H.; Itoh, K. M.; Shutthanandan, V.; Wiggins, P. A.; Fu, K.-M. C. Wide-Field Dynamic Magnetic Microscopy Using Double-Double Quantum Driving of a Diamond Defect Ensemble. *Phys. Rev. Appl.* **2021**, *15*, 054032.
(67) Demas, V.; Lowery, T. J. Magnetic resonance for in vitro medical diagnostics: superparamagnetic nanoparticle-based magnetic relaxation switches. *New J. Phys.* **2011**, *13*, 025005.
(68) Mahmoudi, M.; Sant, S.; Wang, B.; Laurent, S.; Sen, T. Superparamagnetic iron oxide nanoparticles (SPIONs): Development, surface modification and applications in chemotherapy. *Adv. Drug Delivery Rev.* **2011**, *63*, 24.
(69) Orwa, J.; Ganesan, K.; Newnham, J.; Santori, C.; Barclay, P.; Fu, K.; Beausoleil, R.; Aharonovich, I.; Fairchild, B.; Olivero, P.; Greentree, A.; Prawer, S. An upper limit on the lateral vacancy diffusion length in diamond. *Diamond Relat. Mater.* **2012**, *24*, 6.

https://doi.org/10.1021/acsnano.3c12283
ACS Nano 2024, 18, 6523−6532